Flux-controlled skin effect and topological transition in a dissipative two-leg ladder model

Chaohua Wu [ORCID],[1] Zhesen Yang,[2] Jiangshan Tang [ORCID],[3] Ni Liu,[4,5,*] and Gang Chen[1,6,7,†]

[1]*State Key Laboratory of Quantum Optics and Quantum Optics Devices, Institute of Laser Spectroscopy,*
Shanxi University, Taiyuan 030006, China
[2]*Kavli Institute for Theoretical Sciences, University of Chinese Academy of Sciences, Beijing 100190, China*
[3]*College of Engineering and Applied Sciences, National Laboratory of Solid State Microstructures and Collaborative Innovation Center of*
Advanced Microstructures, Nanjing University, Nanjing 210093, China
[4]*Institute of Theoretical Physics, Shanxi University, Taiyuan 030006, China*
[5]*Collaborative Innovation Center of Light Manipulations and Applications, Shandong Normal University, Jinan 250358, China*
[6]*Collaborative Innovation Center of Extreme Optics, Shanxi University, Taiyuan 030006, China*
[7]*School of Physics and Microelectronics, Key Laboratory of Materials Physics of Ministry of Education,*
Zhengzhou University, Zhengzhou 450001, China

The synthetic gauge field and dissipation are of crucial importance in both fundamental physics and applications. Here, we investigate the interplay of the uniform flux and the on-site gain and loss by considering a dissipative two-leg ladder model. By calculating the spectral winding number and the generalized Brillouin zone, we predict the non-Hermitian skin effect, whose skin modes display the bipolar localization. This skin effect emerges when the flux is not an integer multiple of π. We further demonstrate the breakdown of the chiral currents due to the presence of the skin effect by studying single-particle dynamics. Moreover, we show that the non-Hermiticity can drive a flux-dependent topological transition characterized by a hidden Chern number. Our results provide a scheme to manipulate the non-Hermitian skin effect and topological phase transitions, which may find potential applications in lasing, light manipulating, and signal processing.

I. INTRODUCTION

Non-Hermitian systems, described by Hamiltonians with non-Hermitian terms, have attracted significant attention both theoretically and experimentally in recent years [1–6]. In general, there are two kinds of non-Hermitian Hamiltonians, describing on-site gain-loss and nonreciprocal systems. They host extensive properties with no correspondence to Hermitian systems, such as complex eigenvalues [7], biorthonormal eigenvectors [8], and exceptional points [9]. A most intriguing feature is the non-Hermitian skin effect [10–22], where the non-Hermiticity drives the bulk eigenstates of the system to approach the boundaries. It leads to potential applications, including lasing [23–25], sensing [26,27], directional amplification [28,29], and anomalous transport behavior [30–36]. Recently, the interplay of non-Hermiticity and topology was explored [37] and led to novel topological invariants [38–44], non-Bloch bulk-boundary correspondence [45–51], and rich topological classifications with new symmetries [52–55].

Meanwhile, the discovery of a synthetic gauge field involving neutral entities has revolutionized the field of quantum simulation [56–69]. A simple and archetypal model to study the effect of the synthetic gauge field is the two-leg ladder lattice subjected to a flux in each square plaquette. It was demonstrated experimentally in ultracold atoms [70–74] and photonics [75] that the flux can induce spin-momentum locking in the band structure, chiral currents, and Meissner-to-vortex phase transition. In these experimental systems, on-site dissipations are also well controlled. Thus, it is natural to ask what interesting physics will occur under the interplay between the synthetic gauge field and non-Hermiticity. Recent work [76] considered a non-Hermitian two-leg ladder model with staggered flux and parity-time ($\mathcal{PT}$) symmetry on-site gain and loss. It was shown that such a system does not exhibit the non-Hermitian skin effect and the non-Hermitian parameters do not affect the topological phases.

In this paper, we consider a dissipative two-leg ladder model with uniform flux (complex hoppings) and anti-$\mathcal{PT}$-symmetry on-site gain and loss. It is found that the non-Hermitian skin effect appears when the flux is not an integer multiple of π. In particular, the skin modes display bipolar localization, which can be characterized by the spectral winding number and the generalized Brillouin zone (GBZ). We further demonstrate the breakdown of the chiral currents due to the presence of the skin effect by studying single-particle dynamics. We also reveal that the non-Hermiticity can induce a flux-dependent topological transition, which is characterized by a hidden Chern number. Our results provide a scheme to steer skin effects and study non-Hermitian topological states, which may find applications in lasing, light manipulation, and signal processing.

---

*Corresponding author: liuni2011520@sxu.edu.cn
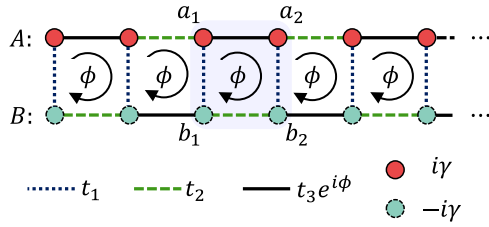†Corresponding author: chengang971@163.com

FIG. 1. Schematic of the non-Hermitian two-leg (labeled A and B) ladder model with four sites $\{a_{1,2}, b_{1,2}\}$ per unit cell (shaded region). t_1 (dotted lines) is the interleg coupling strength, and t_2 (dashed lines) and $t_3 e^{i\phi}$ (solid lines) are the intraleg couplings, which generate a flux ϕ threading each square plaquette. The sites of the A and B legs are subjected to on-site gain (solid red circles) and loss (dashed green circles), respectively.

II. MODEL AND HAMILTONIAN

Figure 1 shows our introduced non-Hermitian two-leg (labeled A and B) ladder model with four sites $\{a_{1,2}, b_{1,2}\}$ per unit cell (shaded region), where a and b denote the A and B legs, respectively, and 1 and 2 denote two sublattices within a unit cell in each leg. This model hosts the interleg coupling strength t_1 (dotted lines) and the intraleg couplings t_2 (dashed lines) and $t_3 e^{i\phi}$ (solid lines). As a result, each plaquette is threaded by a synthetic magnetic flux ϕ. On the other hand, the sites of the A and B legs are subjected to on-site gain (solid red circles) and loss (dashed green circles), respectively. The gain and loss rates are denoted by γ. The corresponding tight-binding Hamiltonian is given by

$$H = \sum_{j}^{N} \{[-t_1(a_{j,1}^\dagger b_{j,1} + b_{j,2}^\dagger a_{j,2}) - t_2(b_{j,1}^\dagger b_{j,2} + a_{j,2}^\dagger a_{j+1,1})$$
$$- t_3 e^{i\phi}(a_{j,2}^\dagger a_{j,1} + b_{j,2}^\dagger b_{j+1,1}) + \text{H.c.}]$$
$$+ i\gamma(a_{j,1}^\dagger a_{j,1} - b_{j,1}^\dagger b_{j,1} - b_{j,2}^\dagger b_{j,2} + a_{j,2}^\dagger a_{j,2})\}, \quad (1)$$

where $\alpha_{j,s}$ and $\alpha_{j,s}^\dagger$ are the annihilation and creation operators on the α-s sublattice of the jth unit cell with $\alpha = a$ or b and $s = 1$ or 2; $L = 4N$ is the length of the lattice, with N being the number of the unit cells; and H.c. represents the Hermitian conjugate. The third line of Eq. (1) describes the non-Hermitian part with on-site gain and loss.

In the basis of $(a_{1,k}, b_{1,k}, b_{2,k}, a_{2,k})^{\mathrm{T}}$, the Hamiltonian (1) is written as

$$H(k) = \begin{pmatrix} i\gamma & -t_1 & 0 & h_1 \\ -t_1 & -i\gamma & h_2 & 0 \\ 0 & h_2^* & -i\gamma & -t_1 \\ h_1^* & 0 & -t_1 & i\gamma \end{pmatrix}, \quad (2)$$

with $h_1 = -t_3 e^{-i\phi} - t_2 e^{-ik}$ and $h_2 = -t_2 - t_3 e^{-i\phi} e^{-ik}$. The Hamiltonian (2) satisfies a pseudo-anti-Hermiticity (i.e., non-Hermitian chiral symmetry), $H(k) = -\Gamma H^\dagger(k)\Gamma$, with $\Gamma = \sigma_0 \otimes \sigma_z$. This symmetry can induce a nontrivial topology with pairwise eigenvalues with $E(k) = -E^*(k)$ [77]. For $\phi = 0$, the Hamiltonian (2) possesses particle-hole symmetry with $\Gamma H^*(k)\Gamma^{-1} = -H(-k)$ and anti-$\mathcal{PT}$ symmetry $(\mathcal{PT})H(k)(\mathcal{PT})^{-1} = -H(k)$, with $\mathcal{P} = i\sigma_x \otimes \sigma_y$ and $\mathcal{T} = \mathcal{K}$ being the complex-conjugation operator. Here, σ_0 is the 2×2

identity matrix, and $\sigma_{x,y,z}$ are the Pauli matrices. Due to the presence of the flux, the system does not have time-reversal symmetry.

In fact, the Hamiltonian (1) can be viewed as a non-Hermitian generalized Su-Schrieffer-Heeger (SSH) model with next-nearest-neighbor intercell coupling [78,79]. It should be noted that a similar non-Hermitian generalized SSH model with a synthetic gauge field was discussed in Ref. [76] which is equivalent to a two-leg ladder lattice with staggered flux and $\mathcal{PT}$-symmetry on-site gain and loss. That paper demonstrated that such staggered flux affects the topological phase of the system, which does not exhibit the non-Hermitian skin effect. Moreover, the non-Hermiticity determines the $\mathcal{PT}$-symmetry transition, while it does not affect the topological phase transitions. Intriguingly, the dissipative two-leg model considered here exhibits quite different properties under the interplay of the uniform flux and anti-$\mathcal{PT}$-symmetry on-site gain and loss. In the following, we will demonstrate that the dissipative two-leg ladder model with uniform flux hosts the non-Hermitian skin effect and show the breakdown of the chiral dynamics due to the interaction between chiral currents induced by the gauge field and skin effect. We will also reveal a flux-dependent topological phase transition induced solely by the on-site gain and loss.

III. NON-HERMITIAN SKIN EFFECT

In this section, we demonstrate that the dissipative two-leg ladder shown in Fig. 1 exhibits the non-Hermitian skin effect under the interplay of the flux and on-site gain and loss.

A typical signature of the non-Hermitian skin effect is the significant difference in the energy spectra in the complex plane of the non-Hermitian Hamiltonian under the open boundary condition (OBC) and the periodic boundary condition (PBC). In Figs. 2(a)–2(e), we plot the complex energy spectra of the Hamiltonian (1) with $\gamma = 0.5$ for $\phi = 0$, $\phi = \pi/4$, $\phi = \pi/2$, $\phi = 3\pi/4$, and $\phi = \pi$, respectively. It is found that the energy spectra under the OBC and PBC totally overlap for $\phi = 0$ [Fig. 2(a)] and $\phi = \pi$ [Fig. 2(e)]. However, for $\phi = \pi/4$, $\pi/2$, and $3\pi/4$ [Figs. 2(b)–2(d)], the PBC spectra form two closed loops, which are separated from those under the OBC. These results indicate that the system sustains the skin effect when $\gamma \neq 0$ and $\phi \neq n\pi$, with n being the integer number.

To further clarify the existence of the skin effect, in Figs. 2(f)–2(j) we show the profiles of all eigenstates as a function of eigenenergies corresponding to Figs. 2(a)–2(e) under the OBC. It is clear that all eigenstates are distributed among the bulk for $\phi = 0$ [Fig. 2(f)] and $\phi = \pi$ [Fig. 2(j)]. However, for $\phi = \pi/4$, $\pi/2$, and $3\pi/4$ [Figs. 2(g)–2(i)], the eigenstates with $\text{Re}(E) > 0$ are localized at the left boundary of the ladder, while the eigenstates with $\text{Re}(E) < 0$ are accumulated at the right boundary. This phenomenon is the so-called bipolar non-Hermitian skin effect [80–82], where the eigenstates collapse to both ends of the lattice. Note that there are several extended eigenstates with $\text{Re}(E) \approx 0$ for $\phi = \pi/4$ and $\pi/2$. These energies are dubbed the Bloch points, which belong to both the PBC and OBC spectra.

The non-Hermitian skin effect is a consequence of the nontrivial topology of a point-gapped non-Hermitian system,
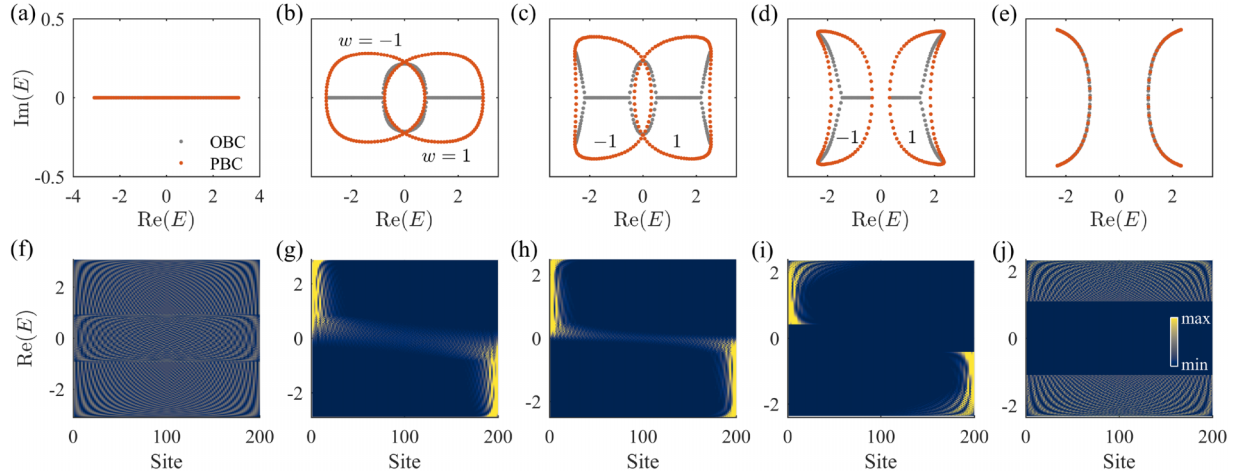
FIG. 2. Complex energy spectra of the Hamiltonian (1) under the OBC (gray dots) and the PBC (red dots) for (a) $\phi = 0$, (b) $\phi = \pi/4$, (c) $\phi = \pi/2$, (d) $\phi = 3\pi/4$, and (e) $\phi = \pi$. $w = \pm 1$ denotes the wingding number of the eigenvalues under the PBC. (f)–(j) Profiles of all eigenstates as a function of eigenenergies corresponding to (a)–(e). The other parameters are chosen to be $t_1 = 1.2$, $t_2 = t_3 = 1$, $\gamma = 0.5$, and $N = 50$. We set $t_2 = 1$ as the energy unit.

which can be characterized by the spectral winding number [13]. The spectral winding number with respect to a reference energy E_r is defined as

$$w = \sum_{m=1}^{M} \oint_{\text{BZ}} \frac{dk}{2\pi} \partial_k \arg[E_m(k) - E_r], \qquad (3)$$

where $E_m(k)$ is the eigenenergy of the Bloch Hamiltonian (2), M is the total number of bands, and the integral runs over the whole Brillouin zone. Equation (3) means that the non-Hermitian skin effect presents in the system under the OBC if w is nonzero with respect to a certain reference energy E_r. Moreover, the sign of w determines the skin direction of the eigenstates; that is, a positive (negative) sign indicates the localization to the left (right). By calculating the spectral winding number of the Hamiltonian (2), we obtain $w = -1$ (clockwise winding) for the bands with $\text{Re}(E) < 0$ and $w = 1$ (counterclockwise winding) for the bands with $\text{Re}(E) > 0$, as shown in Figs. 2(b)–2(d). Therefore, the eigenstates with $\text{Re}(E) < 0$ under the OBC are localized on the right side of the ladder, and the eigenstates with $\text{Re}(E) > 0$ are localized on the left side, which is consistent with Figs. 2(g)–2(i). For the Hermitian case, or $\phi = n\pi$, the complex spectra under the PBC collapse into lines or arcs [Figs. 2(a) and 2(e)], and there is no skin effect.

The properties of the above non-Hermitian skin effect can also be characterized by the GBZ [46,47], which is calculated by

$$f(\beta, E) = \det[E - H(\beta)] = 0, \qquad (4)$$

with $H(\beta) = H(e^{ik} \to \beta)$ and E being the eigenvalues under the OBC. Here, $f(\beta, E)$ is a quartic equation for β (see Appendix A for details), having four solutions β_i ($i = 1, \dots, 4$), with $|\beta_1| \leqslant |\beta_2| \leqslant |\beta_3| \leqslant |\beta_4|$. The trajectory of solution β satisfying $|\beta_2| = |\beta_3|$ gives rise to the GBZ.

Figures 3(a) and 3(b) show the GBZs of the Hamiltonian (1) for $\phi = \pi/2$ and $\phi = 3\pi/4$, respectively. It can be seen that one set of sub-GBZs with $\text{Re}(E) > 0$ (purple dots) is located in the interior of the unit circle (gray lines), indi-

cating the localization on the left end. However, another set of sub-GBZs with $\text{Re}(E) < 0$ (red dots) is outside the unit circle, indicating the localization on the right end. Especially, the intersections of the GBZ with the unit circle [Fig. 3(a)] correspond to the Bloch points.

IV. INTERPLAY OF CHIRAL DYNAMICS AND SKIN EFFECT

From the above discussions, such a flux-dependent dissipative two-leg model displays the bipolar non-Hermitian skin effect. Contrary to the conventional single-side skin effect, the wave dynamics exhibits ballisticlike transport instead of the directional bulk flow for arbitrary single-site initial excitation of the system. This makes the detection of the bipolar non-Hermitian skin effect experimentally challenging. On the other hand, we note that one of the hallmark features of the Hermitian two-leg ladder model with magnetic flux (Hall ladder) is the chiral current [70,71]. In this section, we study the interplay of the chiral current and non-Hermitian skin effect.

In the absence of non-Hermiticity ($\gamma = 0$) and $t_2 = t_3$, the Hamiltonian (1) reduces to the general two-legged ladder with
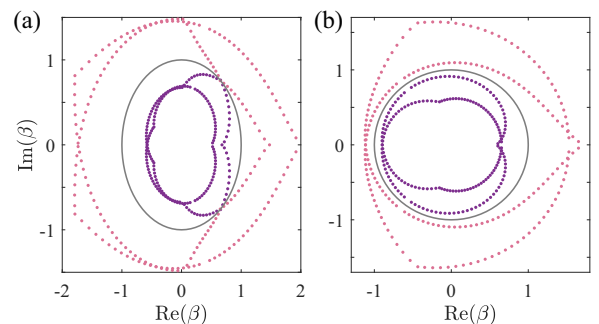

FIG. 3. The generalized Brillouin zone (red and purple dots) of the Hamiltonian (1) for (a) $\phi = \pi/2$ and (b) $\phi = 3\pi/4$. The other parameters are the same as those in Fig. 2. The gray line is the unit circle.
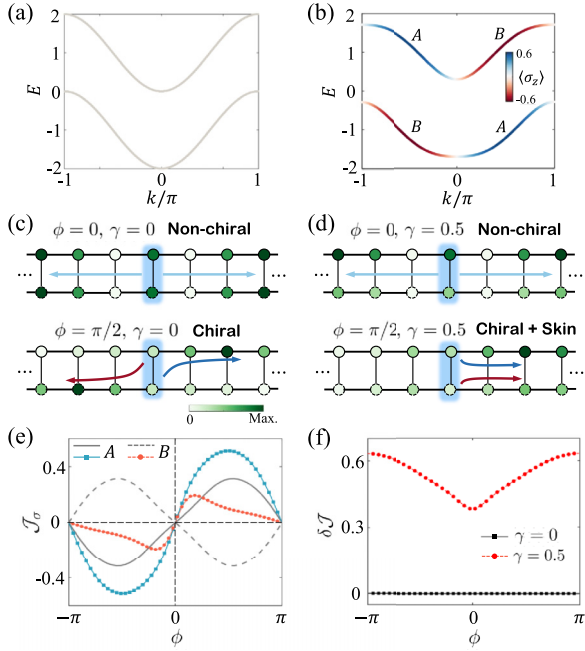
FIG. 4. (a) Band structure of the Hamiltonian (5) for $\phi = 0$. (b) Chiral band structure of the Hamiltonian (5) for $\phi = \pi/2$. The color represents spin polarization $\langle \sigma_z \rangle$ for corresponding eigenstates and indicates on which leg (A or B) the eigenstates mainly locate. In (a) and (b), we choose $\gamma = 0$ and $t_1/t_2 = 0.5$ and set $t_2 = 1$ as the energy unit. (c) Numerical results of the density distributions at time $t = 4$ for $\{\phi = 0, \gamma = 0\}$ (top panel) and $\{\phi = \pi/2, \gamma = 0\}$ (bottom panel). The blue shaded regions denote the single-particle initial state occupying the central rung subsystem with symmetric superposition. The color of a given circle indicates the occupation probability of that lattice site. (d) Numerical results of the density distributions at time $t = 4$ for $\{\phi = 0, \gamma = 0.5\}$ (top panel) and $\{\phi = \pi/2, \gamma = 0.5\}$ (bottom panel). (e) The chiral currents $\mathcal{J}_\sigma$ as a function of ϕ at times in (c) and (d) for $\gamma = 0$ [solid gray (dashed gray) line for $\sigma = A$ ($\sigma = B$)] and $\gamma = 0.5$ [blue line with squares (red line with circles) for $\sigma = A$ ($\sigma = B$)]. (f) The population differences $\delta \mathcal{J}$ between the A and B legs as a function of ϕ at times in (c) and (d) for $\gamma = 0$ (red line with circles) and $\gamma = 0.5$ (black line with squares), respectively. In (c)–(f), the wave functions of the system are normalized.

two sites per unit cell, which is a simplified version of the Harper-Hofstadter model. In this case, Eq. (2) becomes

$$H_T(k) = -2t_2[\sigma_0 \cos(\phi/2) \cos(k)$$
$$+ \sigma_z \sin(\phi/2) \sin(k)] - t_1 \sigma_x. \quad (5)$$

The flux allows us to engineer an analog of "spin-momentum locking" in such a ladder structure.

In Figs. 4(a) and 4(b), we plot the band structures of $H_T(k)$ with the "spin texture" $\langle \sigma_z \rangle$ (color) for $\phi = 0$ and $\phi = \pi/2$, respectively. For $\phi = 0$ [Fig. 4(a)], the bands exhibit no chirality with $\langle \sigma_z \rangle = 0$. However, for $\phi = \pi/2$ [Fig. 4(b)], an interesting correlation between the dispersion and $\langle \sigma_z \rangle$ emerges. For example, in the lower band, the eigenstates that have a positive (negative) dispersion concentrate on the A (B) leg, while the upper band exhibits the opposite case. This is the essence of the chiral edge currents; that is, excitations on different edges or with different spin states move in op-

posite directions. We study the single-particle dynamics to demonstrate the chiral currents of this system. In the limit that $t_1 > t_2 > 0$, we can excite the lower band by choosing an initial state with symmetric superposition on the central rung sites [blue shaded region in Figs. 4(c) and 4(d)], which is the ground state of the isolated rung subsystem [69]. We then investigate the propagation dynamics of the system under this initial state. Figure 4(c) shows the density distributions at time $t = 4$ with $\gamma = 0$ for $\phi = 0$ and $\phi = \pi/2$. At zero flux [top panel of Fig. 4(c)], the wave packet travels to the left and to the right from the initial rung with symmetric trajectories. However, for $\phi = \pi/2$ [bottom panel of Fig. 4(c)], the population demonstrates asymmetric propagation through which rightward (leftward) motion is correlated with a bias towards the A (B) leg of the ladder, as illustrated by the blue (red) arrow. This indicates the chiral dynamics is associated with the chiral bands. Figure 4(c) also shows that the group velocities of the wave-packet evolution are different for $\phi = 0$ and $\phi = \pi/2$. This is because the bands of $\phi = 0$ have a steeper dispersion (i.e., a larger group velocity) compared to $\phi = \pi/2$, as shown in Figs. 4(a) and 4(b). Remarkably, by choosing the initial state with antisymmetric superposition on the central rung sites, we can excite the upper band shown in Fig. 4(b), giving rises to the opposite case. Here, we focus on the symmetric initial state.

We now consider the effects of dissipation with $\gamma = 0.5$. As shown in the upper panel of Fig. 4(d), when $\phi = 0$, the population is symmetric about the initial rung without chirality. However, for $\phi = \pi/2$, the system exhibits the non-Hermitian skin effect, which significantly influences the chiral dynamics. From Sec. III, the eigenstates of the lower band with $\text{Re}(E) < 0$ are localized on the right side of the open system, which may hinder the chiral dynamics. As shown in the bottom panel of Fig. 4(d), the populations for both the upper and lower legs are moved in the right direction, which is dramatically different from the bottom panel of Fig. 4(c). To quantify the amount of chirality, we define the chiral current as

$$\mathcal{J}_\sigma = \mathcal{P}_{R,\sigma} - \mathcal{P}_{L,\sigma}, \quad (6)$$

where $\mathcal{P}_{d,\sigma}$ ($d \in L, R, \sigma = A, B$) denotes the total population at the σ leg in half of the system (L, left; R, right) with respect to the central rung. Figure 4(e) shows the calculated $\mathcal{J}_\sigma$ versus the phase ϕ for $\gamma = 0$ and $\gamma = 0.5$. For $\gamma = 0$, $\mathcal{J}_A$ and $\mathcal{J}_B$ are symmetric around $\mathcal{J}_\sigma = 0$ with $\mathcal{J}_A + \mathcal{J}_B = 0$. However, for $\gamma = 0.5$, $\mathcal{J}_A$ and $\mathcal{J}_B$ have the same sign at the same ϕ. From these results, it is found that the combination of the dissipation ($\gamma \neq 0$) and flux ($\phi \neq n\pi$, with n being the integer number) causes the breakdown of the chiral dynamics due to the presence of the non-Hermitian skin effect, which can be conveniently captured by the single-particle dynamics. Note that, due to the different dissipation rates of the two legs, the population between the A and B legs is not symmetric, as shown in Fig. 4(d). This can be described by defining the population difference between the A and B legs, i.e., $\delta \mathcal{J} = \mathcal{P}_A - \mathcal{P}_B$, where $\mathcal{P}_\sigma$ denotes the total population at the σ leg. Figure 4(f) shows $\delta \mathcal{J}$ as a function of ϕ for $\gamma = 0$ (black line with squares) and $\gamma = 0.5$ (red line with circles). One can find that $\delta \mathcal{J} > 0$ and varies with ϕ for $\gamma = 0.5$, indicating the unbalanced population between these two legs.
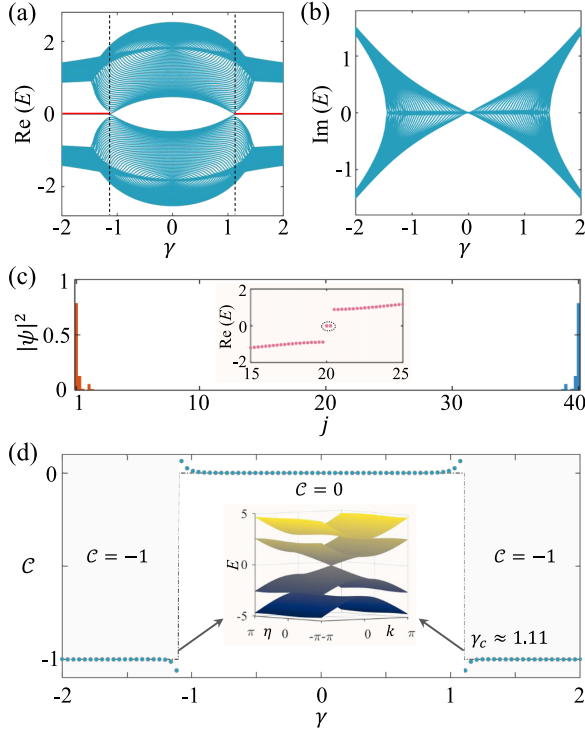
FIG. 5. The (a) real and (b) imaginary parts of the energy spectrum of the Hamiltonian (1) as a function of γ for $t_1 = 1.5$, $t_2 = 1$, $t_3 = 0.2$, $\phi = \pi/2$, and $N = 40$, with $t_2 = 1$ being taken as the unit of energies. (c) The distribution of the twofold-degenerate edge states [$\text{Re}(E) = 0$] with $\gamma = 2$. The inset shows the corresponding real-energy spectrum. (d) The calculated hidden Chern number $\mathcal{C}$ (blue dots) as a function of γ with the same parameters as in (a) and (b). The inset shows the band structure of the Hamiltonian (7) at $\gamma_c \approx \pm 1.11$.

V. NON-HERMITICITY-INDUCED TOPOLOGICAL INSULATING PHASE

In this section, we show that the non-Hermitian on-site gain and loss can drive the system from the trivial to topological insulating phases, which is associated with the flux. It should be emphasized that, unlike the general model of non-Hermiticity-induced topological transitions [77,83–86], the conventional Bloch band theory is not applicable here due to the non-Hermitian skin effect.

In Figs. 5(a) and 5(b), we plot the real and imaginary parts of the energy spectrum under the OBC as a function of γ with $t_1 = 1.5$, $t_2 = 1$, $t_3 = 0.2$, and $\phi = \pi/2$. We see that as $|\gamma|$ increases, the bulk gap closes and reopens (the small derivation arises from the finite-size effect) at a critical point $\gamma_c \approx \pm 1.11$ (black dashed lines), leading to a topological phase transition with the emergence of two midgap states with $\text{Re}(E) = 0$ (red lines). The density distributions of these two midgap edge states are well localized at the boundary of the ladder, as shown in Fig. 5(c).

For non-Hermitian systems without the skin effect, it has been shown that the topology can be described by introducing the complex Berry phase in the k space. However, for systems with the non-Hermitian skin effect and sublattice symmetry, the topology can be explored through the GBZ (non-Bloch
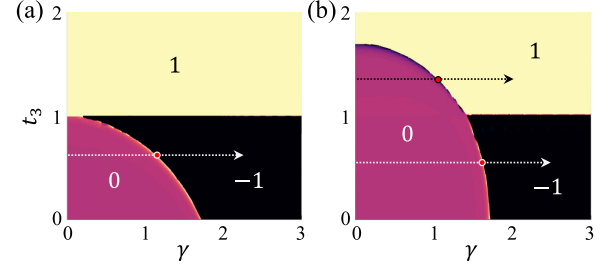

FIG. 6. Phase diagrams of $\mathcal{C}$ in the γ-t_3 plane with $t_1 = 2$ and $t_2 = 1$ for (a) $\phi = 0$ and (b) $\phi = \pi/2$, respectively. Each phase is associated with a value of the Chern number taking the values $\mathcal{C} = \{0, \pm 1\}$.

winding number). Instead of considering the complex GBZ in Fig. 3, here, we show that a hidden Chern number can be used to characterize the emergence of a topological phase transition in Fig. 5(a). This Chern number is described by an effective two-dimensional Hermitian Hamiltonian involving the imaginary part of the energy [87].

For a one-dimensional non-Hermitian chiral-symmetric Hamiltonian, i.e., $H(k) = -\Gamma H^\dagger(k) \Gamma$, the topology can be captured by the corresponding effective Hermitian Hamiltonian $\mathcal{H}(k, \eta) = \Gamma[\eta - iH(k)]$, with η being the imaginary part of the eigenenergies, which holds for both the absence and presence of the non-Hermitian skin effect. From Eq. (2), the effective Hermitian Hamiltonian is obtained as

$$\mathcal{H}(k, \eta) = \begin{pmatrix} \eta + \gamma & it_1 & 0 & -ih_1 \\ -it_1 & -\eta + \gamma & ih_2 & 0 \\ 0 & -ih_2 & \eta - \gamma & it_1 \\ ih_1 & 0 & -it_1 & -\eta - \gamma \end{pmatrix}. \quad (7)$$

Accordingly, a Chern number can be defined in the two-dimensional (k-η) space. To overcome the antiperiodicity in the η direction, we define $\mathcal{H}'(k, \eta) = R_\eta \mathcal{H}(k, \eta) R_\eta^\dagger$, with $R_\eta = \exp[i\frac{\pi}{4}(1 + \tanh \eta)\mathcal{G}]$ and $\mathcal{G} = \sigma_x \otimes \sigma_0$. In this case, $\mathcal{H}'(k, \eta \to -\infty) = \mathcal{H}'(k, \eta \to +\infty) = -|\eta|\Gamma$ as $R_{-\infty} = \sigma_0 \otimes \sigma_0$ and $R_{+\infty} = i\mathcal{G}$ [87]. Then, the Chern number of $\mathcal{H}'(k, \eta)$ can be obtained as

$$\mathcal{C} = \frac{1}{2\pi} \int_{-\infty}^{+\infty} d\eta \int_{-\pi}^{\pi} dk \, \Omega_{k,\eta}, \quad (8)$$

with the Berry curvature

$$\Omega_{k,\eta} = \sum_{\substack{m \leqslant 2 \\ m' > 2}} \text{Im} \frac{2 \langle \psi_{k,\eta}^m | \partial_k \mathcal{H}' | \psi_{k,\eta}^{m'} \rangle \langle \psi_{k,\eta}^{m'} | \partial_\eta \mathcal{H}' | \psi_{k,\eta}^m \rangle}{(E_{k,\eta}^m - E_{k,\eta}^{m'})}. \quad (9)$$

Here, $|\psi_{k,\eta}^m\rangle$ are the eigenstates of $\mathcal{H}'(k, \eta)$ with energies $E_{k,\eta}^m$.

In Fig. 5(d), we numerically calculate $\mathcal{C}$ (blue dots) as a function of γ. It is clear that a topological transition from $\mathcal{C} = 0$ to $\mathcal{C} = -1$ emerges at $\gamma_c \approx \pm 1.11$, which agrees with those in Fig. 5(a). At the critical point γ_c, the middle two bands of $\mathcal{H}'$ close at $(k = 0, \eta = 0)$. Note that $\mathcal{H}'$ and $\mathcal{H}$ have the same energy spectrum. According to bulk-boundary correspondence, the zero-energy edge states can also be obtained from the Hamiltonian $\mathcal{H}$ under the OBC, i.e., $\mathcal{H}_{\text{obc}}$ (see Appendix B).

In Figs. 6(a) and 6(b), we plot the hidden Chern numbers $\mathcal{C}$ in the γ-t_3 plane for $\phi = 0$ and $\phi = \pi/2$, respectively. One
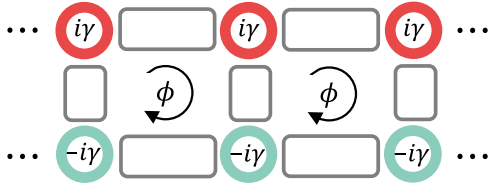
FIG. 7. Experimental implementation of the Hamiltonian (1) in Fig. 1 using coupled-ring-resonator arrays. The gain (loss) sites are denoted by the red (green) rings. The neighboring main resonators are coupled by link resonators (gray rings).

can observe that the non-Hermiticity can drive a topological transition from $\mathcal{C} = 0$ to $\mathcal{C} = -1$ when $\phi = 0$. However, for $\phi = \pi/2$, it can induce transitions from $\mathcal{C} = 0$ to $\mathcal{C} = \pm1$. The topological phase diagram can be changed by tuning the flux. In fact, these topological phases and transitions are related to the corresponding topological phases of the Hermitian case. As mentioned above, the Hamiltonian (1) describes a long-range SSH model with winding numbers $w = \{0, \pm1\}$ [76]. The non-Hermiticity induces a topological insulating phase if $\{t_1, t_2, t_3\}$ is chosen in the trivial phase ($w = 0$).

VI. POSSIBLE EXPERIMENTAL IMPLEMENTATION

The key points of the experiment are to realize the flux and on-site dissipations. A possible experimental generation of such a dissipative two-leg ladder model can be achieved in arrays of coupled ring resonators [61,88–90], as shown in Fig. 7. Within this system, each site is represented by a main ring resonator (in red or green), which is coupled to its neighboring resonators through antiresonant link rings (in gray). The amplitudes of the coupling strengths between the lattice sites are controlled by adjusting the gap between the site-ring and link-ring waveguides. The link rings can be used to manipulate the phase of the coupling between the site rings and introduce a synthetic gauge flux threading each square plaquette. Specifically, when the link ring coupling two site rings is vertically shifted, the photons hopping towards the right travel a slightly longer path compared to those hopping towards the left. This path length difference results in an effective hopping phase ϕ. In an active photonic platform, the on-site loss comes from the intrinsic material loss without pumping, while the gain is obtained by external pumping [91]. In the experiment, the spatial intensity profile in the ladder can be directly imaged by using a microscope objective and an infrared camera. To probe the presence of topological edge states in the ladder, we can fabricate a waveguide coupler at the end of the ladder and measure the power absorption at this location as a function of the laser frequency.

It should be noticed that the physics discussed above are also present in a loss-only system, i.e., a nonactive system. In addition to the coupled arrays of ring resonators, other platforms such as ultracold atoms [69,73], superconducting circuits [92–94], electric circuits [95–100], and photonic resonator networks with synthetic dimensions [75,101] are also promising systems for investigating the physical effects discussed here.

VII. CONCLUSION

In summary, we have studied the non-Hermitian skin effect and topological phase of a dissipative two-leg ladder model with a uniform flux on each plaquette. The skin effect emerges when the flux is not an integer multiple of π in the presence of nonvanishing dissipation, displaying bipolar localization. By studying the single-particle dynamics, we have also demonstrated the breakdown of the chiral currents due to the presence of the skin effect. Moreover, we have shown that the non-Hermiticity can drive a flux-dependent topological transition from trivial to topological phases, which can be characterized by a hidden Chern number. Our paper may pave the way for the study of the non-Hermitian skin effect and non-Hermitian topological states and provides potential applications in tunable lasers, light manipulation, and signal processing.

APPENDIX A: THE EXPRESSION OF $f(\beta, E)$

Based on Eqs. (2) and (4), we obtain

$$f(\beta, E) = \sum_{n=0}^{4} r_n \beta^n, \tag{A1}$$

with

$$r_0 = r_4 = t_2^2 t_3^2, \tag{A2}$$

$$r_1 = 2\cos(\phi)\left(t_2^3 t_3 + t_2 t_3^3 + t_2 t_3 \gamma^2 - E^2 t_2 t_3\right) \\ - t_1^2 t_2^2 - t_1^2 t_3^2 + 4E t_2 t_3 \gamma \sin(\phi), \tag{A3}$$

$$r_2 = E^4 + t_1^4 + t_2^4 + t_3^4 + 2\gamma^2\left(E - t_1^2 + t_2^2 + t_3^2\right) \\ + 2t_2^2 t_3^2 [1 + \cos(2\phi)] - 2E^2\left(t_1^2 + t_2^2 + t_3^2\right) \\ + \gamma^4 - 4t_1^2 t_2 t_3 \cos(\phi), \tag{A4}$$

$$r_3 = 2\cos(\phi)\left(t_2^3 t_3 + t_2 t_3^3 + t_2 t_3 \gamma^2 - E^2\right) - t_1^2 t_2^2 \\ - t_1^2 t_3^2 - 4E t_2 t_3 \gamma \sin(\phi). \tag{A5}$$

By substituting the eigenvalues E under the OBC into $f(\beta, E) = 0$, one can get four solutions of β_i with $|\beta_1| \leqslant |\beta_2| \leqslant |\beta_3| \leqslant |\beta_4|$. The GBZ is given by the trajectory of β_2 and β_3 satisfying $|\beta_2| = |\beta_3|$.

APPENDIX B: THE ENERGY SPECTRUM OF $\mathcal{H}_{\mathbf{obc}}$

In this Appendix, we show that the topological edge state in Fig. 5(a) can also be clarified by the effective Hamiltonian (7). If $\mathcal{H}(k, \eta)$ is topological with a nontrivial Chern number, boundary modes crossing the energy gap under the OBC exist.
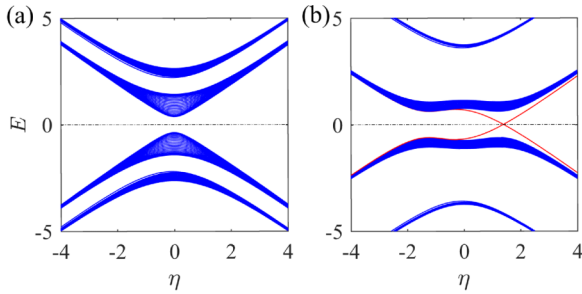
(a)
(b)

FIG. 8. The energy spectra of Eq. (B1) as a function of η for (a) $\gamma = 0.5$ and (b) $\gamma = 2$. The dot-dashed lines denote the zero-energy level, and the red lines denote the in-gap boundary states. The other parameters are the same as those in Fig. 5.

The open boundary Hamiltonian of $\mathcal{H}(k, \eta)$ is given by [87]

$$\mathcal{H}_{\text{obc}} = \Gamma_{\text{obc}}[\eta - iH_{\text{obc}}], \tag{B1}$$

where $\Gamma_{\text{obc}} = \mathbb{I}_N \otimes \Gamma$, with $\mathbb{I}_N$ being the $N \times N$ identity matrix, and H_{obc} is the corresponding open boundary Hamiltonian of $H(k)$.

In Fig. 8, we plot the energy spectra of $\mathcal{H}_{\text{obc}}$ for $\gamma = 0.5$ and $\gamma = 2$. We see that, for the trivial case [Fig. 8(a)], there are no boundary states in the energy gap. However, in the nontrivial case [Fig. 8(b)], two states (red lines) appear in the middle gap. They cross the zero-energy level at the same values of η, which corresponds to the two degenerate edge states of H_{obc}. These results agree with those in Fig. 5.

[1] N. Moiseyev, *Non-Hermitian Quantum Mechanics* (Cambridge University Press, Cambridge, 2011).

[2] V. V. Konotop, J. Yang, and D. A. Zezyulin, Nonlinear waves in $\mathcal{PT}$-symmetric systems, Rev. Mod. Phys. **88**, 035002 (2016).

[3] C. M. Bender, Making sense of non-Hermitian Hamiltonians, Rep. Prog. Phys. **70**, 947 (2007).

[4] R. El-Ganainy, K. G. Makris, M. Khajavikhan, Z. H. Musslimani, S. Rotter, and D. N. Christodoulides, Non-Hermitian physics and PT symmetry, Nat. Phys. **14**, 11 (2018).

[5] Ş. K. Özdemir, S. Rotter, F. Nori, and L. Yang, Parity-time symmetry and exceptional points in photonics, Nat. Mater. **18**, 783 (2019).

[6] Y. Ashida, Z. Gong, and M. Ueda, Non-Hermitian physics, Adv. Phys. **69**, 249 (2020).

[7] K. Wang, A. Dutt, C. C. Wojcik, and S. Fan, Topological complex-energy braiding of non-Hermitian bands, Nature (London) **598**, 59 (2021).

[8] D. C. Brody, Biorthogonal quantum mechanics, J. Phys. A **47**, 035305 (2014).

[9] M.-A. Miri and A. Alù, Exceptional points in optics and photonics, Science **363**, eaar7709 (2019).

[10] S. Yao and Z. Wang, Edge States and Topological Invariants of Non-Hermitian Systems, Phys. Rev. Lett. **121**, 086803 (2018).

[11] S. Longhi, Probing non-Hermitian skin effect and non-Bloch phase transitions, Phys. Rev. Res. **1**, 023013 (2019).

[12] K. Zhang, Z. Yang, and C. Fang, Correspondence between Winding Numbers and Skin Modes in Non-Hermitian Systems, Phys. Rev. Lett. **125**, 126402 (2020).

[13] Z. Gong, Y. Ashida, K. Kawabata, K. Takasan, S. Higashikawa, and M. Ueda, Topological Phases of Non-Hermitian Systems, Phys. Rev. X **8**, 031079 (2018).

[14] L. Li, C. H. Lee, S. Mu, and J. Gong, Critical non-Hermitian skin effect, Nat. Commun. **11**, 5491 (2020).

[15] R. Okugawa, R. Takahashi, and K. Yokomizo, Second-order topological non-Hermitian skin effects, Phys. Rev. B **102**, 241202(R) (2020).

[16] T. Helbig, T. Hofmann, S. Imhof, M. Abdelghany, T. Kiessling, L. W. Molenkamp, C. H. Lee, A. Szameit, M. Greiter, and R. Thomale, Generalized bulk-boundary correspondence in non-Hermitian topolectrical circuits, Nat. Phys. **16**, 747 (2020).

[17] N. Okuma, K. Kawabata, K. Shiozaki, and M. Sato, Topological Origin of Non-Hermitian Skin Effects, Phys. Rev. Lett. **124**, 086801 (2020).

[18] L. Li, C. H. Lee, and J. Gong, Topological Switch for Non-Hermitian Skin Effect in Cold-Atom Systems with Loss, Phys. Rev. Lett. **124**, 250402 (2020).

[19] Y. Yi and Z. Yang, Non-Hermitian Skin Modes Induced by On-Site Dissipations and Chiral Tunneling Effect, Phys. Rev. Lett. **125**, 186802 (2020).

[20] Z. Lin, L. Ding, S. Ke, and X. Li, Steering non-Hermitian skin modes by synthetic gauge fields in optical ring resonators, Opt. Lett. **46**, 3512 (2021).

[21] Y. Li, C. Liang, C. Wang, C. Lu, and Y.-C. Liu, Gain-Loss-Induced Hybrid Skin-Topological Effect, Phys. Rev. Lett. **128**, 223903 (2022).

[22] Q. Liang, D. Xie, Z. Dong, H. Li, H. Li, B. Gadway, W. Yi, and B. Yan, Dynamic Signatures of Non-Hermitian Skin Effect and Topology in Ultracold Atoms, Phys. Rev. Lett. **129**, 070401 (2022).

[23] B. Bahari, A. Ndao, F. Vallini, A. E. Amili, Y. Fainman, and B. Kanté, Nonreciprocal lasing in topological cavities of arbitrary geometries, Science **358**, 636 (2017).

[24] M. Parto, S. Wittek, H. Hodaei, G. Harari, M. A. Bandres, J. Ren, M. C. Rechtsman, M. Segev, D. N. Christodoulides, and M. Khajavikhan, Edge-Mode Lasing in 1D Topological Active Arrays, Phys. Rev. Lett. **120**, 113901 (2018).

[25] B. Zhu, Q. Wang, D. Leykam, H. Xue, Q. J. Wang, and Y. D. Chong, Anomalous Single-Mode Lasing Induced by Nonlinearity and the Non-Hermitian Skin Effect, Phys. Rev. Lett. **129**, 013903 (2022).

[26] J. C. Budich and E. J. Bergholtz, Non-Hermitian Topological Sensors, Phys. Rev. Lett. **125**, 180403 (2020).

[27] A. McDonald and A. A. Clerk, Exponentially-enhanced quantum sensing with non-Hermitian lattice dynamics, Nat. Commun. **11**, 5382 (2020).

[28] C. C. Wanjura, M. Brunelli, and A. Nunnenkamp, Topological framework for directional amplification in driven-dissipative cavity arrays, Nat. Commun. **11**, 3149 (2020).

[29] C. C. Wanjura, M. Brunelli, and A. Nunnenkamp, Correspondence between Non-Hermitian Topology and Directional Amplification in the Presence of Disorder, Phys. Rev. Lett. **127**, 213601 (2021).

[30] S. Weidemann, M. Kremer, T. Helbig, T. Hofmann, A. Stegmaier, M. Greiter, R. Thomale, and A. Szameit, Topological funneling of light, Science **368**, 311 (2020).

[31] S. Weidemann, M. Kremer, S. Longhi, and A. Szameit, Coexistence of dynamical delocalization and spectral localization through stochastic dissipation, Nat. Photonics **15**, 576 (2021).

[32] C. Wu, J. Fan, G. Chen, and S. Jia, Non-Hermiticity-induced reentrant localization in a quasiperiodic lattice, New J. Phys. **23**, 123048 (2021).

[33] F. Song, S. Yao, and Z. Wang, Non-Hermitian Skin Effect and Chiral Damping in Open Quantum Systems, Phys. Rev. Lett. **123**, 170401 (2019).

[34] C.-H. Liu, K. Zhang, Z. Yang, and S. Chen, Helical damping and dynamical critical skin effect in open quantum systems, Phys. Rev. Res. **2**, 043167 (2020).

[35] S. Longhi, Non-Bloch-Band Collapse and Chiral Zener Tunneling, Phys. Rev. Lett. **124**, 066602 (2020).

[36] S. Longhi, Self-Healing of Non-Hermitian Topological Skin Modes, Phys. Rev. Lett. **128**, 157601 (2022).

[37] E. J. Bergholtz, J. C. Budich, and F. K. Kunst, Exceptional topology of non-Hermitian systems, Rev. Mod. Phys. **93**, 015005 (2021).

[38] T. E. Lee, Anomalous Edge State in a Non-Hermitian Lattice, Phys. Rev. Lett. **116**, 133903 (2016).

[39] S. Yao, F. Song, and Z. Wang, Non-Hermitian Chern Bands, Phys. Rev. Lett. **121**, 136802 (2018).

[40] D. Leykam, K. Y. Bliokh, C. Huang, Y. D. Chong, and F. Nori, Edge Modes, Degeneracies, and Topological Numbers in Non-Hermitian Systems, Phys. Rev. Lett. **118**, 040401 (2017).

[41] H. Jiang, C. Yang, and S. Chen, Topological invariants and phase diagrams for one-dimensional two-band non-Hermitian systems without chiral symmetry, Phys. Rev. A **98**, 052116 (2018).

[42] A. Ghatak and T. Das, New topological invariants in non-Hermitian systems, J. Phys.: Condens. Matter **31**, 263001 (2019).

[43] S. Lieu, Topological phases in the non-Hermitian Su-Schrieffer-Heeger model, Phys. Rev. B **97**, 045106 (2018).

[44] C. Yin, H. Jiang, L. Li, R. Lü, and S. Chen, Geometrical meaning of winding number and its characterization of topological phases in one-dimensional chiral non-Hermitian systems, Phys. Rev. A **97**, 052115 (2018).

[45] H. Shen, B. Zhen, and L. Fu, Topological Band Theory for Non-Hermitian Hamiltonians, Phys. Rev. Lett. **120**, 146402 (2018).

[46] K. Yokomizo and S. Murakami, Non-Bloch Band Theory of Non-Hermitian Systems, Phys. Rev. Lett. **123**, 066404 (2019).

[47] Z. Yang, K. Zhang, C. Fang, and J. Hu, Non-Hermitian Bulk-Boundary Correspondence and Auxiliary Generalized Brillouin Zone Theory, Phys. Rev. Lett. **125**, 226402 (2020).

[48] F. K. Kunst, E. Edvardsson, J. C. Budich, and E. J. Bergholtz, Biorthogonal Bulk-Boundary Correspondence in Non-Hermitian Systems, Phys. Rev. Lett. **121**, 026808 (2018).

[49] L. Jin and Z. Song, Bulk-boundary correspondence in a non-Hermitian system in one dimension with chiral inversion symmetry, Phys. Rev. B **99**, 081103(R) (2019).

[50] L. Xiao, T. Deng, K. Wang, G. Zhu, Z. Wang, W. Yi, and P. Xue, Non-Hermitian bulk-oundary correspondence in quantum dynamics, Nat. Phys. **16**, 761 (2020).

[51] T.-S. Deng and W. Yi, Non-Bloch topological invariants in a non-Hermitian domain wall system, Phys. Rev. B **100**, 035102 (2019).

[52] H. Zhou and J. Y. Lee, Periodic table for topological bands with non-Hermitian symmetries, Phys. Rev. B **99**, 235112 (2019).

[53] K. Kawabata, K. Shiozaki, M. Ueda, and M. Sato, Symmetry and Topology in Non-Hermitian Physics, Phys. Rev. X **9**, 041015 (2019).

[54] K. Kawabata, S. Higashikawa, Z. Gong, Y. Ashida, and M. Ueda, Topological unification of time-reversal and particle-hole symmetries in non-Hermitian physics, Nat. Commun. **10**, 297 (2019).

[55] C.-H. Liu, H. Jiang, and S. Chen, Topological classification of non-Hermitian systems with reflection symmetry, Phys. Rev. B **99**, 125103 (2019).

[56] M. Aidelsburger, M. Atala, S. Nascimbène, S. Trotzky, Y.-A. Chen, and I. Bloch, Experimental Realization of Strong Effective Magnetic Fields in an Optical Lattice, Phys. Rev. Lett. **107**, 255301 (2011).

[57] J. Dalibard, F. Gerbier, G. Juzeliūnas, and P. Öhberg, Colloquium: Artificial gauge potentials for neutral atoms, Rev. Mod. Phys. **83**, 1523 (2011).

[58] A. Celi, P. Massignan, J. Ruseckas, N. Goldman, I. B. Spielman, G. Juzeliūnas, and M. Lewenstein, Synthetic Gauge Fields in Synthetic Dimensions, Phys. Rev. Lett. **112**, 043001 (2014).

[59] L. Barbiero, C. Schweizer, M. Aidelsburger, E. Demler, N. Goldman, and F. Grusdt, Coupling ultracold matter to dynamical gauge fields in optical lattices: From flux attachment to $\mathbb{Z}_2$ lattice gauge theories, Sci. Adv. **5**, eaav7444 (2019).

[60] K. Fang, Z. Yu, and S. Fan, Realizing effective magnetic field for photons by controlling the phase of dynamic modulation, Nat. Photonics **6**, 782 (2012).

[61] M. Hafezi, S. Mittal, J. Fan, A. Migdall, and J. M. Taylor, Imaging topological edge states in silicon photonics, Nat. Photonics **7**, 1001 (2013).

[62] M. Schmidt, S. Kessler, V. Peano, O. Painter, and F. Marquardt, Optomechanical creation of magnetic fields for photons on a lattice, Optica **2**, 635 (2015).

[63] Y. Lumer, M. A. Bandres, M. Heinrich, L. J. Maczewsky, H. Herzig-Sheinfux, A. Szameit, and M. Segev, Light guiding by artificial gauge fields, Nat. Photonics **13**, 339 (2019).

[64] E. Lustig, S. Weimann, Y. Plotnik, Y. Lumer, M. A. Bandres, A. Szameit, and M. Segev, Photonic topological insulator in synthetic dimensions, Nature (London) **567**, 356 (2019).

[65] M. Aidelsburger, M. Atala, M. Lohse, J. T. Barreiro, B. Paredes, and I. Bloch, Realization of the Hofstadter Hamiltonian with Ultracold Atoms in Optical Lattices, Phys. Rev. Lett. **111**, 185301 (2013).

[66] M. Mancini, G. Pagano, G. Cappellini, L. Livi, M. Rider, J. Catani, C. Sias, P. Zoller, M. Inguscio, M. Dalmonte, and L. Fallani, Observation of chiral edge states with neutral fermions in synthetic Hall ribbons, Science **349**, 1510 (2015).

[67] B. K. Stuhl, H.-I. Lu, L. M. Aycock, D. Genkina, and I. B. Spielman, Visualizing edge states with an atomic Bose gas in the quantum Hall regime, Science **349**, 1514 (2015).

[68] M. Aidelsburger, M. Lohse, C. Schweizer, M. Atala, J. T. Barreiro, S. Nascimbene, N. Cooper, I. Bloch, and

N. Goldman, Measuring the Chern number of Hofstadter bands with ultracold bosonic atoms, Nat. Phys. **11**, 162 (2015).

[69] M. E. Tai, A. Lukin, M. Rispoli, R. Schittko, T. Menke, D. Borgnia, P. M. Preiss, F. Grusdt, A. M. Kaufman, and M. Greiner, Microscopy of the interacting Harper-Hofstadter model in the two-body limit, Nature (London) **546**, 519 (2017).

[70] D. Hügel and B. Paredes, Chiral ladders and the edges of quantum Hall insulators, Phys. Rev. A **89**, 023619 (2014).

[71] M. Atala, M. Aidelsburger, M. Lohse, J. Barreiro, B. Paredes, and I. Bloch, Observation of chiral currents with ultracold atoms in bosonic ladders, Nat. Phys. **10**, 588 (2014).

[72] L. F. Livi, G. Cappellini, M. Diem, L. Franchi, C. Clivati, M. Frittelli, F. Levi, D. Calonico, J. Catani, M. Inguscio, and L. Fallani, Synthetic Dimensions and Spin-Orbit Coupling with an Optical Clock Transition, Phys. Rev. Lett. **117**, 220401 (2016).

[73] F. A. An, E. J. Meier, and B. Gadway, Direct observation of chiral currents and magnetic reflection in atomic flux lattices, Sci. Adv. **3**, e1602685 (2017).

[74] J. H. Han, D. Bae, and Y. Shin, Synthetic Hall ladder with tunable magnetic flux, Phys. Rev. A **105**, 043306 (2022).

[75] A. Dutt, Q. Lin, L. Yuan, M. Minkov, M. Xiao, and S. Fan, A single photonic cavity with two independent physical synthetic dimensions, Science **367**, 59 (2020).

[76] L. Du, J.-H. Wu, M. Artoni, and G. C. L. Rocca, Phase-dependent topological interface state and spatial adiabatic passage in a generalized Su-Schrieffer-Heeger model, Phys. Rev. A **100**, 012112 (2019).

[77] K. Takata and M. Notomi, Photonic Topological Insulating Phase Induced Solely by Gain and Loss, Phys. Rev. Lett. **121**, 213902 (2018).

[78] S.-L. Zhang and Q. Zhou, Two-leg Su-Schrieffer-Heeger chain with glide reflection symmetry, Phys. Rev. A **95**, 061601(R) (2017).

[79] M. Maffei, A. Dauphin, F. Cardano, M. Lewenstein, and P. Massignan, Topological characterization of chiral models through their long time dynamics, New J. Phys. **20**, 013023 (2018).

[80] F. Song, S. Yao, and Z. Wang, Non-Hermitian Topological Invariants in Real Space, Phys. Rev. Lett. **123**, 246801 (2019).

[81] L. Zhang, Y. Yang, Y. Ge, Y.-J. Guan, Q. Chen, Q. Yan, F. Chen, R. Xi, Y. Li, D. Jia, S.-Q. Yuan, H.-X. Sun, H. Chen, and B. Zhang, Acoustic non-Hermitian skin effect from twisted winding topology, Nat. Commun. **12**, 6297 (2021).

[82] L. Li and C. H. Lee, Non-Hermitian pseudo-gaps, Sci. Bull. **67**, 685 (2022).

[83] H. C. Wu, L. Jin, and Z. Song, Topology of an anti-parity-time symmetric non-Hermitian Su-Schrieffer-Heeger model, Phys. Rev. B **103**, 235110 (2021).

[84] X.-W. Luo and C. Zhang, Higher-Order Topological Corner States Induced by Gain and Loss, Phys. Rev. Lett. **123**, 073601 (2019).

[85] C. Wu, N. Liu, G. Chen, and S. Jia, Non-Hermiticity-induced topological transitions in long-range Su-Schrieffer-Heeger models, Phys. Rev. A **106**, 012211 (2022).

[86] Y. Ao, X. Hu, Y. You, C. Lu, Y. Fu, X. Wang, and Q. Gong, Topological Phase Transition in the Non-Hermitian Coupled Resonator Array, Phys. Rev. Lett. **125**, 013902 (2020).

[87] W. Brzezicki and T. Hyart, Hidden Chern number in one-dimensional non-Hermitian chiral-symmetric systems, Phys. Rev. B **100**, 161105(R) (2019).

[88] M. Hafezi, E. A. Demler, M. D. Lukin, and J. M. Taylor, Robust optical delay lines with topological protection, Nat. Phys. **7**, 907 (2011).

[89] D. Leykam, S. Mittal, M. Hafezi, and Y. D. Chong, Reconfigurable Topological Phases in Next-Nearest-Neighbor Coupled Resonator Lattices, Phys. Rev. Lett. **121**, 023901 (2018).

[90] S. Mittal, V. V. Orre, G. Zhu, M. A. Gorlach, A. Poddubny, and M. Hafezi, Photonic quadrupole topological phases, Nat. Photonics **13**, 692 (2019).

[91] H. Zhao, X. Qiao, T. Wu, B. Midya, S. Longhi, and L. Feng, Non-Hermitian topological light steering, Science **365**, 1163 (2019).

[92] R. Ma, B. Saxberg, C. Owens, N. Leung, Y. Lu, J. Simon, and D. I. Schuster, Nature (London) **566**, 51 (2019).

[93] X. Guan, Y. Feng, Z.-Y. Xue, G. Chen, and S. Jia, Synthetic gauge field and chiral physics on two-leg superconducting circuits, Phys. Rev. A **102**, 032610 (2020).

[94] C. Wu, X. Guan, J. Fan, G. Chen, and S. Jia, Dynamical characterization of quadrupole topological phases in superconducting circuits, Phys. Rev. A **104**, 022601 (2021).

[95] C. H. Lee, S. Imhof, C. Berger, F. Bayer, J. Brehm, L. W. Molenkamp, T. Kiessling, and R. Thomale, Topolectrical circuits, Commun. Phys. **1**, 39 (2018).

[96] D. Zou, T. Chen, W. He, J. Bao, C. H. Lee, H. Sun, and X. Zhang, Observation of hybrid higher-order skin-topological effect in non-Hermitian topolectrical circuits, Nat. Commun. **12**, 7201 (2021).

[97] S. Liu, R. Shao, S. Ma, L. Zhang, O. You, H. Wu, Y. J. Xiang, T. J. Cui, and S. Zhang, Non-Hermitian skin effect in a non-Hermitian electrical circuit, Research **2021**, 5608038 (2021).

[98] A. Stegmaier, S. Imhof, T. Helbig, T. Hofmann, C. H. Lee, M. Kremer, A. Fritzsche, T. Feichtner, S. Klembt, S. Höfling, I. Boettcher, I. C. Fulga, O. G. Schmidt, M. Greiter, T. Kiessling, A. Szameit, and R. Thomale, Topological Defect Engineering and $\mathcal{PT}$ Symmetry in Non-Hermitian Electrical Circuits, Phys. Rev. Lett. **126**, 215302 (2021).

[99] C. Shang, S. Liu, R. Shao, P. Han, X. Zang, X. Zhang, K. N. Salama, W. Gao, C. H. Lee, R. Thomale, A. Manchon, S. Zhang, T. J. Cui, and U. Schwingenschlögl, Experimental identification of the second-order non-Hermitian skin effect with physics-graph-informed machine learning, Adv. Sci. **2202922** (2022).

[100] S. Liu, S. Ma, C. Yang, L. Zhang, W. Gao, Y. J. Xiang, T. J. Cui, and S. Zhang, Gain- and Loss-Induced Topological Insulating Phase in a Non-Hermitian Electrical Circuit, Phys. Rev. Appl. **13**, 014047 (2020).

[101] C. Leefmans, A. Dutt, J. Williams, L. Yuan, M. Parto, F. Nori, S. Fan, and A. Marandi, Topological dissipation in a time-multiplexed photonic resonator network, Nat. Phys. **18**, 442 (2022).